Thermal Deformation Behavior and Constitutive Model Of Hot Isostatically Pressed Superalloy FGH4096

Jianxiao Liu,Chao Jiang,Yuewen Zhai,Leyu Zhou,Zibo Zhang
Beijing Research Institute of Mechanical& Electrical Technology Co.，Ltd. CAM
Room 201, Xueqing Street No.18, HaiDian District, Beijing City, 100083,China
liujianxiao@brimet.ac.cn

Abstract - The thermal deformation behavior of hot isostatically pressed superalloy FGH4096 was investigated by hot compression tests in the range of deformation with 60%, the temperature of 1020~1140°C, and a strain rate of 0.001~1s^{-1}. The stress-strain curves under different deformation conditions were plotted using Origin software, and the relationship between the rheological stress curves and the deformation temperature and strain rate was analyzed. Based on the Arrhenius equation and the Zener-Hollomon parametric model, the high-temperature rheological stress constitutive equation model of HIP-FGH4096 alloy was established, and the heat deformation activation energy was calculated to be $907.348 \text{kJ} \cdot \text{mol}^{-1}$. The Arrhenius-type constitutive equation could predict the flow stress behavior of FGH4096 alloy, the value of the correlation coefficient is 0.98 when the average absolute relative error is 9.21%.

Keywords: Hot isostatically pressed superalloy FGH4096; High-temperature deformation; Constitutive modelling; The apparent activation energy for deformation

1. Introduction

Turbine disk is one of the key components in hot end of an aero-engine when the most demanding and important working conditions [1], Known as the heart of the gas turbine, its metallurgical quality and performance level is decisive for a reliability, safety life and performance improvement of engines and aircraft, and has always received the metallurgists' attention[2][3]. Development of high thrust ratio and high power-to-weight ratio engines has put forward higher requirements for turbine disc toughness, fatigue performance, reliability, and durability[4]. Powdered high-temperature alloy solves the traditional cast and forged high-temperature alloys due to the increase of alloying degree, serious segregation of ingots, poor thermal processing performance, forming difficulties and other problems, is the necessary material for turbine discs and other key components [5][6]. The powdered high-temperature alloys developed at home and abroad have been successfully used in advanced military and civilian aero engines [7].

FGH4096 alloy is a damage-tolerant powder high-temperature alloy which has the advantages of no macroscopic segregation and good resistance to crack expansion and is the preferred material for high-performance turbine discs [8]. This paper intends to explore the thermal deformation stress rheology of FGH4096 powdered high-temperature alloy through thermal simulation experiments to provide theoretical reference and technical support for optimizing the alloying process.

2 Experiment

The test material is FGH4096 nickel-based powdered high-temperature alloy, whose chemical composition is shown in Table 1. The master alloy was made by vacuum induction melting, EIGA atomization powder making, vacuum degassing, and hot isostatic press (HIP) after enveloping. The specimens were machined into cylindrical specimens of $\phi 10 \times 15 \text{mm}$. The isothermal and constant strain rate compression experiments were carried out on a Gleeble-3500 thermal simulation tester with a heating rate of 20 /s ℃, a holding time of 10 min after reaching temperature, deformation temperatures of 1020, 1050, 1080, 1110, 1140 °C, strain rates of 0.001, 0.01, 0.1, 1s^{-1}, and a deformation volume of 60%. The computer autonomously completed the acquisition of relevant data.

Table 1 Chemical compositions of FGH4096 alloy(ω/%)

C	B	Zr	Co	Cr	Mo	W	Ti	Nb	Fe	Si	Al	Ni
0.047	0.015	0.042	13.05	15.86	4.00	3.98	3.77	0.71	0.075	0.025	2.12	余

3 Results and Discussion

3.1 The flow behavior of the HIP-FGH4096 alloy in the isothermal compression process

Based on thermal simulation compression experiments, typical true stress-true strain curves were obtained for this powder metallurgical high-temperature alloy at different deformation temperatures and strain rates. Figure 1 shows the evolution of the rheological stress with true strain, corresponding to strain rates of 0.001s^{-1}, 0.01 s^{-1}, 0.1 s^{-1}, and 1 s^{-1}, respectively.

Overall, at different temperatures and strain rates, the curve trends do not much differ and can be divided into 3 stages: process hardening stage, dynamic softening stage, and dynamic stabilization stage [9]. In the initial stage of deformation, accumulation of dislocations leads to increased process hardening, The rheological stress increases rapidly with the increase of strain, at which time the process hardening dominates and the curve shows a sharp upward trend. As the strain increasing , the rising trend of true stress starts to moderate gradually, which is because with further accumulation of dislocations, the dot matrix distortion energy increases and reaches a critical state, which excites the dynamic recrystallization nucleation and growth, causing the annihilation of dislocations leading to rheological softening phenomenon. After the peak stress appears, as the deformation continues, the flow stress begins to fall and eventually drops to a relatively stable level. The recrystallization phenomenon of the thermal processing process can greatly contribute to the reduction of dislocation density, thus triggering a decrease in rheological stress. Thereafter, even if the strain continues to increase, the flow stress no longer changes, which is due to the generation of stress-strain dynamic equilibrium, showing obviously dynamic stability characteristics.
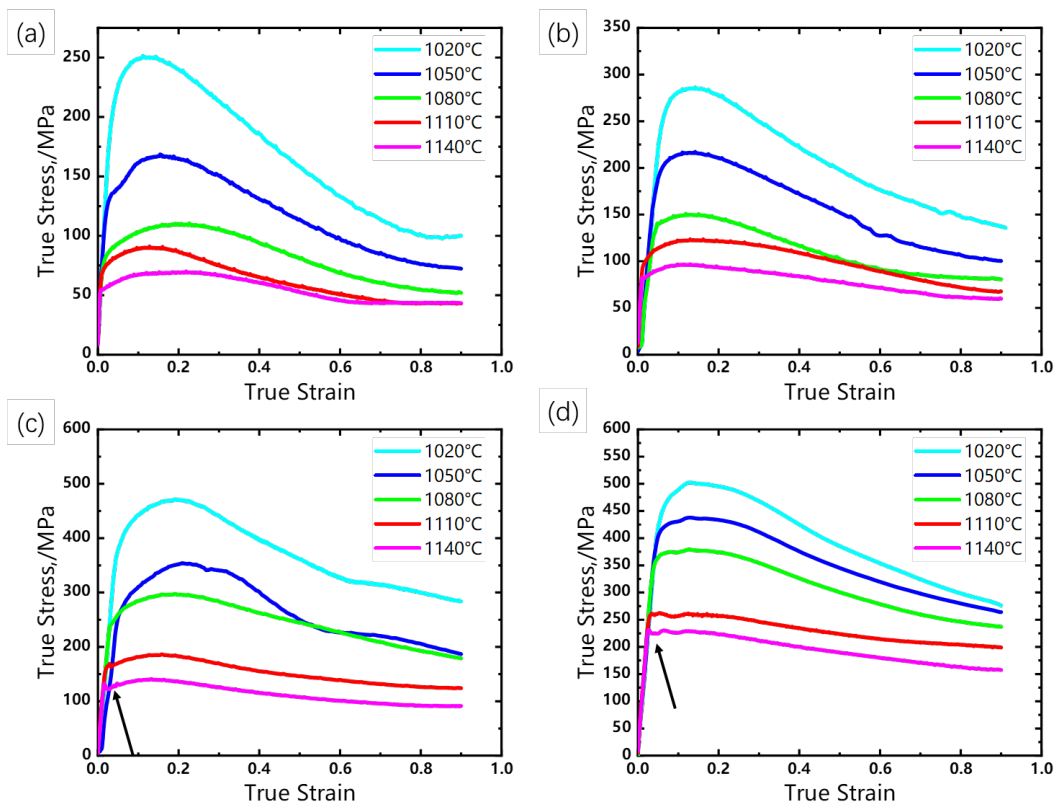

Figure 1 True stress-strain curves of HIP FGH4096 superalloy during hot compression at deformation

(a) 0.001s^{-1}, (b)0.1 s^{-1}, (c)0.1 s^{-1},and(d)1 s^{-1}

At higher deformation temperatures and higher strain rates, there is a significant yield drop in the alloy rheology curve as indicated by the arrow in Figure 1. This is due to the fact that when the alloy is deformed by the slip mechanism, the total macroscopic plastic strain rate is equal to the sum of the strain rates contributed by the individual slip systems due to

dislocation motion. While the density of movable dislocations in initial organization of alloy at high temperatures is low, it increases significantly during plastic deformation at larger strain rates with the opening of multiple slip systems and cross-slip. At a certain strain rate, the speed of dislocation movement decreases with the increase of dislocation density, which leads to a sudden decrease of the critical shear stress and thus the yield landing phenomenon in the rheological curve. At lower temperatures, regardless of high or low strain rates, the alloy does not yield significantly due to increased initial dislocation density, slowed dislocation density growth, and the effect of cross-slip and climbing of some dislocations.

Figure 2 shows the variation of peak stress with temperature for different strain rates. The peak stress increases with increasing strain rate and increases with decreasing temperature. At the same deformation temperature, the probability of dislocation plugging and entanglement gets higher with increasing strain rate, resulting in higher deformation resistance and thus higher rheological stress of the alloy. The effect of strain rate on peak stress is more obvious when in low temperatures, and the difference in peak stress decreases at different temperatures. When the strain rate is constant, as the deformation temperature increases, the bonding force between atoms decreases, and the average kinetic energy of atoms increases, promoting dislocation slip and grain boundary diffusion, leading to a decrease in the dislocation resistance motion affected by thermal activation, resulting in a decrease in rheological stress.
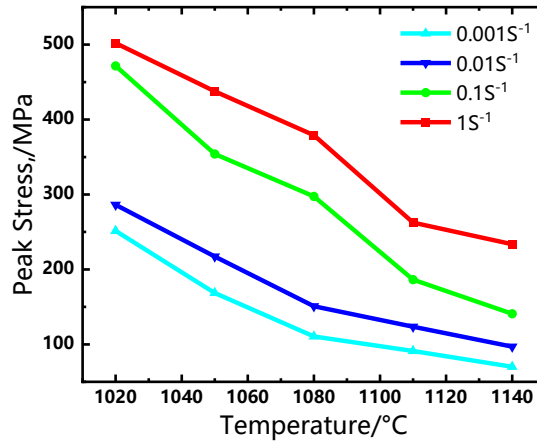

Figure 2 Peak stress as a function of temperature

Higher temperatures and lower strain rates allow dynamic recrystallization grain nucleation and growth to accumulate and move energy more easily at the boundaries, thus reducing rheological stress levels. The flow behavior of alloys is mainly governed by dynamic reversion, dynamic recrystallization, and dislocation mechanisms.

3.2 High-temperature Arrhenius principal structure equation

The intrinsic constitutive equation can be used to predict the rheological stresses in materials with different processing parameters and to describe the rheological behavior of materials during thermal processing.

Sellars and Jonas proposed an intrinsic constitutive equation including deformation activation energy Q and temperature T, namely the Arrhenius equation[10], which is one of the most prevalent models of the intrinsic constitutive equation and has the following three main forms depending on the deformation temperature and stress state: exponential law equation, power law equation, and hyperbolic sine law equation. The expressions can be derived from equations (1) to (3):

$$\dot{\varepsilon} = A_1 \sigma^{n_1} \exp(-Q/RT) \qquad \alpha\sigma < 0.8 \qquad (1)$$

$$\dot{\varepsilon} = A_2 \exp(\beta\sigma)\exp(-Q/RT) \qquad \alpha\sigma > 1.2 \qquad (2)$$

$$\dot{\varepsilon} = A[\sinh(\alpha\sigma)]^n \exp[-Q/(RT)] \qquad \text{for all } \sigma \qquad (3)$$

where T is the thermodynamic temperature (K); R is the gas constant (J·mol^{-1}·K^{-1}), R=8.314kJ/(mol·K); Q is the heat deformation activation energy (kJ·mol^{-1}); $\dot{\varepsilon}$ is the strain rate (s^{-1}); σ is the stress (MPa); A is the structure factor (s^{-1}); α is the stress level parameter (mm^2/N); n and n_1 are the stress index constants; A_1, A_2 and β are material constants, where $A_1 =$

$A/2^{n_1}$, $A_2 = A\alpha^{n_1}$,$\alpha = \beta/n_1$.

    Taking logarithms of both sides of equation (1) at the same time and sorting them:

$$\ln\dot{\varepsilon} = \ln A_1 + n_1 \ln\sigma - Q/(RT) \tag{4}$$

$$n_1 = \frac{\partial \ln\dot{\varepsilon}}{\partial \ln\sigma} \tag{5}$$

    When the temperature is fixed, $\ln\dot{\varepsilon}$ is linearly related to $\ln\sigma$, and n_1 is the slope of the straight line. Substituting each data into the equation and plotting the relationship curve of $\ln\dot{\varepsilon} - \ln\sigma$, as shown in Figure 3, by linear fitting and taking the average value of different temperature slopes, n_1=6.4138.
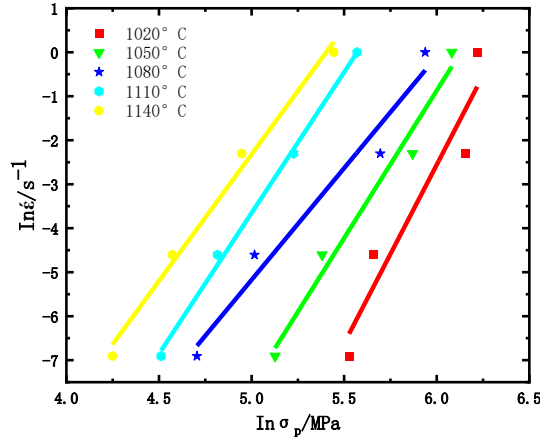
Figure 3 $\ln\dot{\varepsilon} - \ln\sigma$ relationship curves

    Taking the logarithm of both sides of equation (2) at the same time and sorting:

$$\ln\dot{\varepsilon} = \ln A_2 + \beta\sigma - Q/(RT) \tag{6}$$

$$\beta = \frac{\partial \ln\dot{\varepsilon}}{\partial\sigma} \tag{7}$$

    When the temperature is fixed, $\ln\dot{\varepsilon}$ is linearly related to σ, and β is the slope of the straight line. Substituting each data into the equation and plotting the relationship curve of $\ln\dot{\varepsilon} - \sigma$, as shown in Figure 4, by linear fitting and taking the average value of different temperature slopes:$\beta = 0.0297 MPa^{-1}$. $\alpha = \beta/n_1 = 0.0046 MPa^{-1}$.
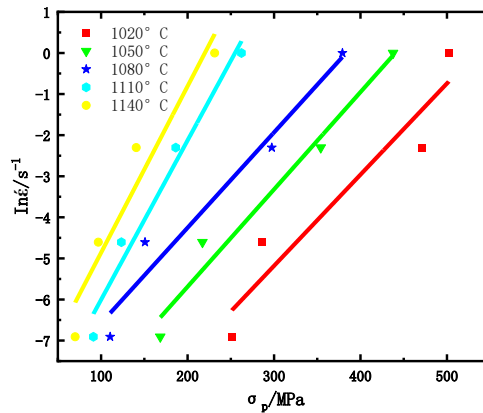

Figure 4 $\ln\dot{\varepsilon} - \sigma$ relationship curves

    Taking the logarithm of both sides of equation (3):

$$\ln\dot{\varepsilon} = \ln A + n\ln[\sin h(\alpha\sigma)] - Q/(RT) \tag{8}$$

Eq. (8) finds the partial derivative of $\dot{\varepsilon}$ and obtains：

$$\frac{\partial\ln[\sinh(\alpha\sigma)]}{\partial\ln\dot{\varepsilon}} = \frac{1}{n} \tag{9}$$

Eq. (8) finds the partial derivative of $\frac{1}{T}$ and obtains：

$$\frac{\partial\ln[\sinh(\alpha\sigma)]}{\partial(\frac{1}{T})} = \frac{Q}{nR} = s \tag{10}$$

Substituting the obtained α values into equation (8), plotting the relationship curve of $ln[\sinh(\alpha\sigma)] - \ln\dot{\varepsilon}$ and $ln[\sinh(\alpha\sigma)] - 1/T$, as shown in Figure 5and Figure 6, it can be seen that $ln[\sinh(\alpha\sigma)]$ has a good linear relationship with both $\ln\dot{\varepsilon}$ and $1/T$ under different conditions. The average slope of the five fitted lines in Fig. 5 is then taken as its inverse to obtain n as 4.7096. A linear fit to the curve in Fig. 6 gives an average slope of 23.172, and the value of S is 2.3172×10^4. Therefore, the heat deformation activation energy of FGH4096 is $Q = s * n * R = 907.348 kJ \cdot mol^{-1}$.
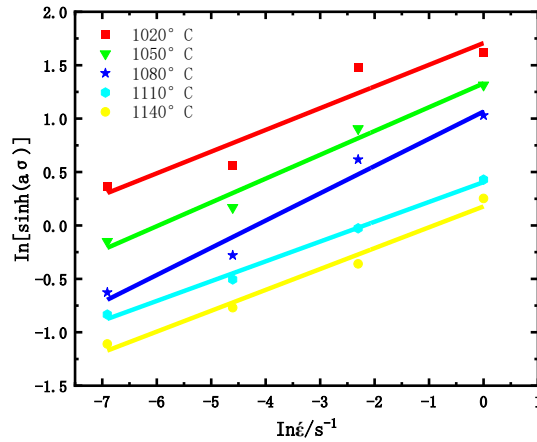

Figure 5 $\ln[\sin h(\alpha\sigma)] - \ln\dot{\varepsilon}$ relationship curves
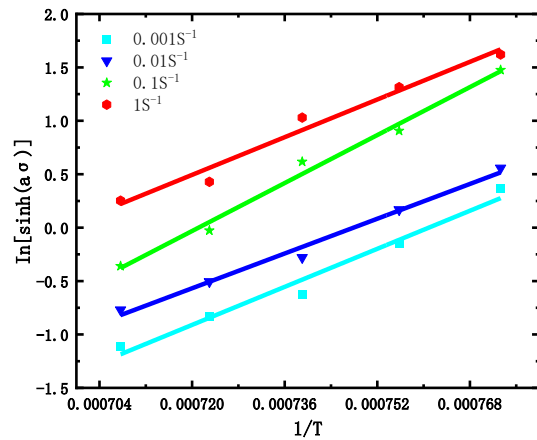

Figure 6 $\ln[\sin h(\alpha\sigma)] - 1/T$ relationship curves

The combined effect of deformation temperature and strain rate on metal forming can be expressed in terms of the Zener-Hollomon parameter[11]，The expression of the Z parameter is as follows:

$$Z = \dot{\varepsilon}\exp(Q/(RT))Z = \dot{\varepsilon}\exp(907.348/(RT)) \tag{11}$$

By combining equation (3) and equation (11):

$$Z = A[\sinh(\alpha\sigma)]^n \tag{12}$$

The deformation activation energy Q is known, and each Z value is found according to the known conditions. Taking logarithms of both sides of equation (12):

$$\ln Z = \ln A + n\ln[\sinh(\alpha\sigma)] \tag{13}$$

The $\ln[\sinh(\alpha\sigma)] - \ln Z$ relationship curve is made according to equation (13), as shown in Figure 7, and lnA is the intercept value of the $\ln[\sinh(\alpha\sigma)] - \ln Z$ curve. The value of lnA is found according to the linear regression method: $A = 1.4314 \times 10^{33}$.
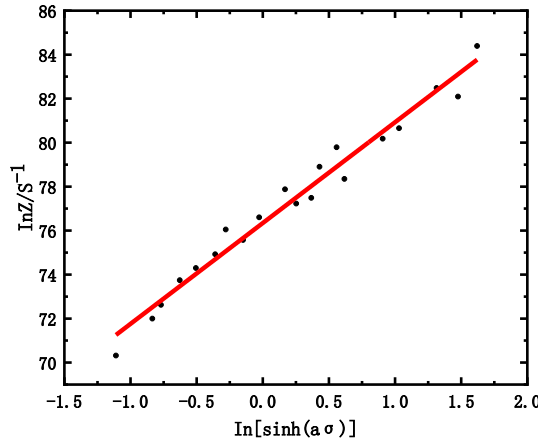

Figure 7 $\ln Z - \ln[\sinh(\alpha\sigma)]$ relationship curves

Substituting the above parameters into equation (3), the Arrhenius hyperbolic sine functional form of FGH4096 and the heat deformation instanton equation with parameter Z values are obtained as follows:

$$\dot{\varepsilon} = 1.4314 * 10^{33}[\sinh(0.0046\sigma)]^{4.7096} \times \exp(907.348/RT) \tag{14}$$

$$\sigma = \frac{1}{0.0046}\ln\left\{\left(\frac{Z}{1.4314*10^{33}}\right)^{1/4.7096} + \left[\left(\frac{Z}{1.4314*10^{33}}\right)^{2/4.7096} + 1\right]^{1/2}\right\} \tag{15}$$

3.3 Strain-fitting modified Arrhenius constitutive equation

It has been shown that the strain has a great influence on the heat deformation activation energy Q and material constants such as α, n, and A. Therefore, in order to establish the full strain principal structure equation, it is necessary to compensate the strain correction for parameters such as Q, α, n, and A. Generally, 1 to 9 times function curves are used to fit the relationship between heat deformation parameters and strain variables[12], and in this paper, the strain interval is selected as 0.05 to 0.9. After analysis, there is a certain nonlinear functional relationship between each material constant and strain variables, and after expressing the material constants in equation (15) as polynomial functions of strain variables, it can be realized to embed the strain variables into the material intrinsic structure relationship and establish the rheological stress instanton equation with coupled strain variables.

Eight times curve fitting was used, as shown in Figure 8. The fitted equation expressions and equation coefficients for each material parameter are shown in equation (16) and Table 2, respectively.

$$\alpha = \alpha_0 + \alpha_1\varepsilon + \alpha_2\varepsilon^2 + \alpha_3\varepsilon^3 + \alpha_4\varepsilon^4 + \alpha_5\varepsilon^5 + \alpha_6\varepsilon^6 + \alpha_7\varepsilon^7 + \alpha_8\varepsilon^8$$
$$n = n_0 + n_1\varepsilon + n_2\varepsilon^2 + n_3\varepsilon^3 + n_4\varepsilon^4 + n_5\varepsilon^5 + n_6\varepsilon^6 + n_7\varepsilon^7 + n_8\varepsilon^8$$
$$Q = Q_0 + Q_1\varepsilon + Q_2\varepsilon^2 + Q_3\varepsilon^3 + Q_4\varepsilon^4 + Q_5\varepsilon^5 + Q_6\varepsilon^6 + Q_7\varepsilon^7 + Q_8\varepsilon^8$$
$$lnA = A_0 + A_1\varepsilon + A_2\varepsilon^2 + A_3\varepsilon^3 + A_4\varepsilon^4 + A_5\varepsilon^5 + A_6\varepsilon^6 + A_7\varepsilon^7 + A_8\varepsilon^8$$
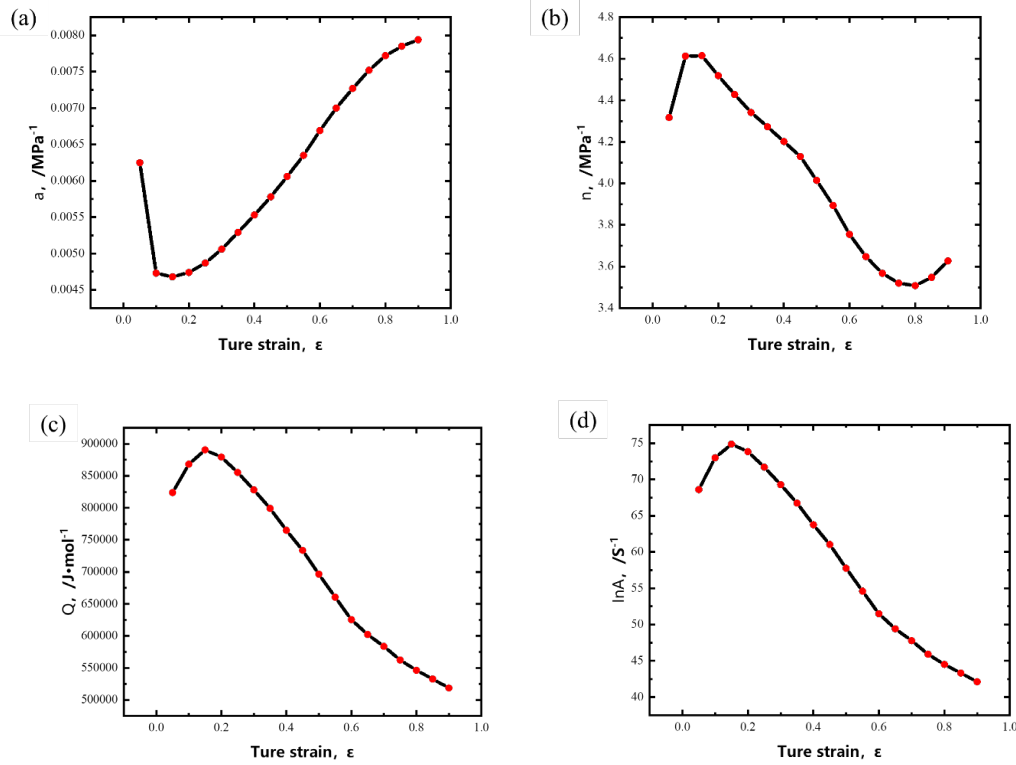
(16)

Figure 8 Relationship of material constants(a)α (b)n (c)Q (d)lnA

Table 2 Fitting coefficients of material constants

a (ε)/ (mm²·N⁻¹)		n (ε)		Q (ε)/(kJ·mol⁻¹)		lnA(ε)/ s⁻¹	
α0	-0.6443	n0	571.6847	Q0	-374064.6631	A0	-31800.0613
α1	2.4040	n1	-1967.1947	Q1	1602946.8954	A1	136634.8421
α2	-3.5704	n2	2578.1158	Q2	-2882808.6442	A2	-246459.9356
α3	2.6312	n3	-1513.5843	Q3	2822027.2204	A3	242048.8538
α4	-0.9397	n4	277.0834	Q4	-1633099.8072	A4	-140559.6618
α5	0.0844	n5	103.5930	Q5	570443.1505	A5	49270.7114
α6	0.0494	n6	-57.7193	Q6	-118492.1378	A6	-10266.8660
α7	-0.0123	n7	7.9310	Q7	13123.4362	A7	1138.6257
α8	0.0054	n8	4.4727	Q8	339.6577	A8	27.1589

The expression for the rheological stress of the material at full strain can be expressed in terms of the Z-parameter, and the experimental full-strain instanton equation is shown in equation (17):

$$\sigma_{(\varepsilon)} = \frac{1}{\alpha_{(\varepsilon)}} \ln\left\{ \left(\frac{Z_{(\varepsilon)}}{A_{(\varepsilon)}}\right)^{1/n_{(\varepsilon)}} + \left[\left(\frac{Z_{(\varepsilon)}}{A_{(\varepsilon)}}\right)^{2/n_{(\varepsilon)}} \right]^{1/2} \right\}$$

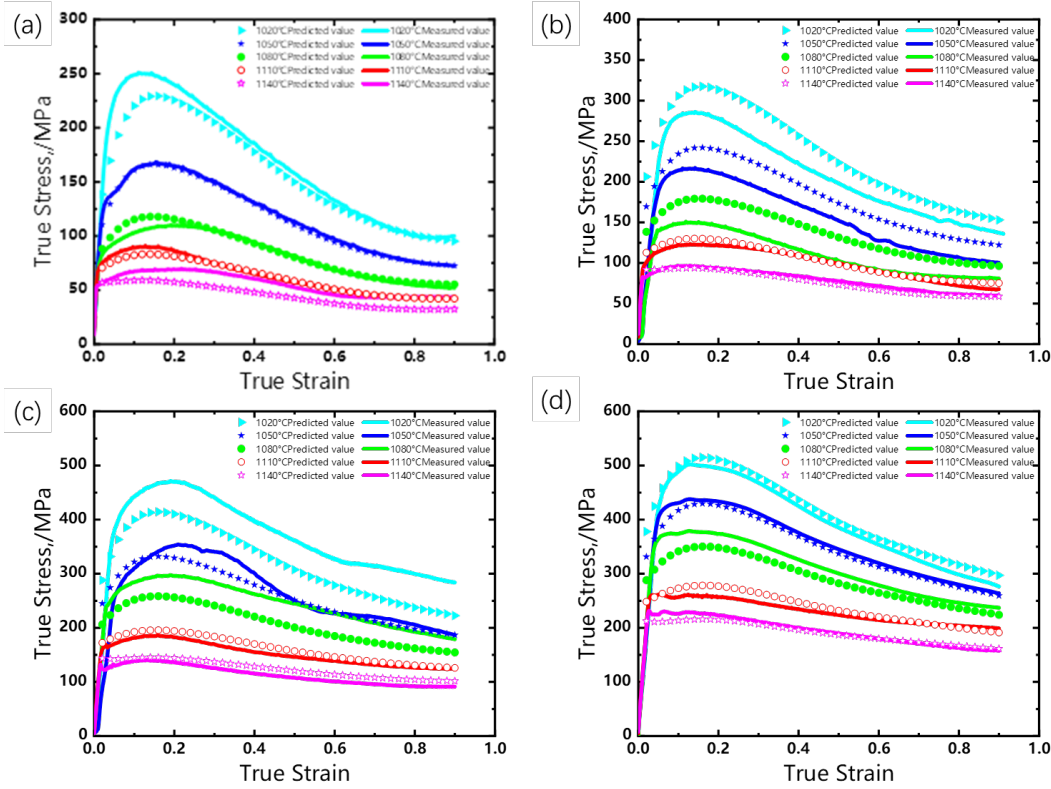$$Z_{(\varepsilon)} = \dot{\varepsilon}\exp\left(\frac{Q_\varepsilon}{RT}\right) \tag{17}$$

Figure 9 Comparison of calculated values and experimental values (a) 0.001s^{-1}, (b)0.1 s^{-1}, (c)0.1 s^{-1},and(d)1 s^{-1}

To verify the correctness and accuracy of the present constitutive equations, the rheological stresses predicted by the present constitutive relationship model for each deformation temperature and strain rate were compared with the data obtained from the hot compression experiments as shown in Figure 9.

To further verify the accuracy of the model, the relationship between the predicted stress and the experimental stress was made as shown inFigure 10. The average relative error AARE and the correlation coefficient R between the predicted and experimental stresses were calculated by Eqs. (18) and (19), respectively[13].

$$AARE = \frac{1}{N}\sum_{i=1}^{N}\left|\frac{E_i - P_i}{E_i}\right| \times 100\% \tag{18}$$

$$R = \frac{\sum_{i=1}^{N}(E_i - E)(P_i - P)}{\sqrt{\sum_{i=1}^{N}(E_i - E)^2 \sum_{i=1}^{N}(P_i - P)^2}} \tag{19}$$

Where: Ei and Pi are the experimental and calculated values of the flow stress; E and P are the average values of the experimental and calculated values of the flow stress; N is the number of points taken.

The average relative error AARE between predicted and experimental stresses was calculated to be 9.21%, and the correlation coefficient R was 0.98. The AARE is an unbiased statistical parameter used to evaluate the predictability of a

model that can be calculated through a term-by-term comparison of relative error. Within the present experimental conditions, the rheological stresses calculated by the model are in good agreement with the experimental values.
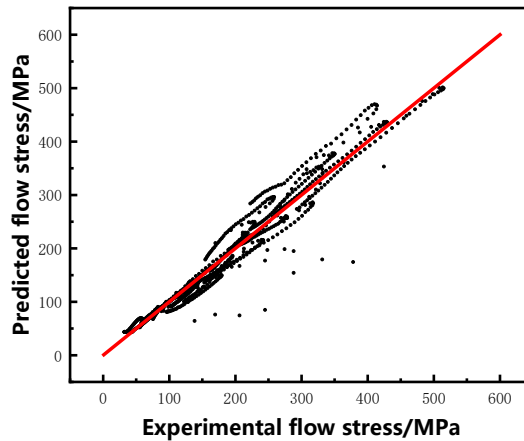

Figure 10 Correlation between experimental values and calculated value

It can be seen that the predicted stresses show a good correlation with the experimental stresses with small errors, which verifies the accuracy of the model. It indicates that the rheological stress instanton equation of FGH4096 alloy with coupled strain variables has high accuracy within the experimental conditions of this paper, and the equation can accurately predict the rheological stress of FGH4096 material under various thermal deformation conditions, reflecting the softening effect of FGH4096 under different compression conditions.

4 Conclusion

1)True stress–true strain curves are the external expression for the result of work hardening combined with thermal dynamic behavior. FGH4096 is a temperature and strain rate sensitive material. Reducing the deformation rate and increasing the deformation temperature can reduce the peak stress of FGH4096 alloy.

2) The initiation of dynamic reversion softening dominated by dislocation motion and recrystallization softening dominated by dynamic recrystallization of grains within the material are the main mechanisms to counteract work hardening.

3) At higher deformation temperatures and higher strain rates, there is a significant yield drop in the alloy rheology curve.

4) The heat deformation activation energy of HIP-FGH4096 alloy is 907.348 kJ/mol, and the heat deformation constitutive equation is obtained by regression analysis as: $\dot{\varepsilon}=1.4314 \times 10^{33}[\sinh(0.0046\sigma)]^{4.7096}\exp(4.7096/RT)$, the fitted correlation coefficient (R) of the model is 0.98 and the average relative error (AARE) is 9.21%, which can predict the actual stress values of the HIP-FGH4096 alloy at different strain rates and deformation temperatures more accurately.

References

[1] Guoqing Zhang,Shifan Tian,Wuxiang Wang,Zhou Li.: Advanced aero-engine turbine disc preparation process and its key technology in China. New Material Industry. 16–21 (2009).

[2] Huanming Chen,Benfu Hu,Yiwen Zhang,Quanmao Yu,Huiying Li.: Research progress of nickel-based powder high-temperature alloy for aircraft turbine discs in China. Materials Guide. 17–19 (2002).

[3] Guoqing Zhang,Yiwen Zhang,Liang Zheng,Zichao Peng.: Research progress of powder high-temperature alloy and preparation technology for aero-engine in China. Journal of Metals. 55, 1133–1144 (2019).

[4] Shuyun Wang,Huiqu Li,Hongtao Yang.: Powdered high-temperature alloy superplasticity isothermal forging technology research in China. Journal of Aerospace Materials. 30–33 (2007).

[5] Yiwen Zhang,Yongheng Shangguan.: Research and Development of Powdered High-Temperature Alloys in China. Powder Metallurgy Industry. 30–43 (2004).

[6] Zhongnan Bi: High-temperature alloy for aero-engine and its preparation technology in China. Large aircraft. 12–15 (2021).

[7] Jinwen Zhou,Wuxiang Wang.:Research progress and application of powdered high-temperature alloys in China. Journal of Aerospace Materials. 244–250 (2006).

[8] Ning, Y., Zhou, C., Liang, H., Fu, M.W.: Abnormal flow behavior and necklace microstructure of powder metallurgy superalloys with previous particle boundaries (PPBs). Mater. Sci. Eng. A. 652, 84–91 (2016).

[9] Ning, Y.Q., Xie, B.C., Zhou, C., Liang, H.Q., Fu, M.W.: Strain-rate sensitivity of powder metallurgy superalloys associated with steady-state DRX during the hot compression process. Met. Mater. Int. 23, 350–358 (2017).

[10] Jonas, J.J., Sellars, C.M., Tegart, W.J.M.: Strength and structure under hot-working conditions. Metall. Rev.

[11] Zener, C., Hollomon, J.H.: Effect of Strain Rate Upon Plastic Flow of Steel. J. Appl. Phys. 15, 22–32 (1944).

[12] Wu, H., Wen, S.P., Huang, H., Wu, X.L., Gao, K.Y., Wang, W., Nie, Z.R.: Hot deformation behavior and constitutive equation of a new type Al–Zn–Mg–Er–Zr alloy during isothermal compression. Mater. Sci. Eng. A. 651, 415–424 (2016)

[13] Huang, C.-Q., Deng, J., Wang, S.-X., Liu, L.: An Investigation on the Softening Mechanism of 5754 Aluminum Alloy during Multistage Hot Deformation. Metals. 7, 107 (2017).